Journal of Catalysis 258 (2008) 131–142

Contents lists available at ScienceDirect

Journal of Catalysis

www.elsevier.com/locate/jcat

Modeling spatially resolved profiles of methane partial oxidation on a Rh foam catalyst with detailed chemistry

D. Dalle Nogare [a,*], N.J. Degenstein [b], R. Horn [b], P. Canu [a], L.D. Schmidt [b]

[a] Department of Chemical Engineering Principles and Practice, University of Padova, Via Marzolo, 9, 35131 Padova, Italy
[b] Department of Chemical Engineering and Materials Science, University of Minnesota, 432 Amundson Hall, 421 Washington Avenue SE, Minneapolis, MN 55455, USA

ARTICLE INFO

Article history:
Received 6 March 2008
Revised 16 May 2008
Accepted 2 June 2008
Available online 10 July 2008

Keywords:
Catalytic partial oxidation
Methane
Foam
Rhodium
Detailed chemistry
Reactor modeling
Transport phenomena
Syngas
Spatial profiles

ABSTRACT

Using spatially resolved measurements of temperature and concentration, we critically analyzed the chemistry and transport limitations in the partial oxidation of methane (POM) reaction carried out on Rh, supported on a foam catalyst. The analysis was based on two models, both sharing a detailed surface chemistry but with different gas–surface transport processes. The simulation neglecting transport limitations correctly predicts the outlet concentrations, apparently because of the approach to equilibrium, but significant disagreement was found along the catalysts, particularly in the initial region, demonstrating the existence of regions in which strong diffusive limitations prevail. We developed a pseudo-1D model that can differentiate the species and temperature in the bulk of the gas and at the surface and describe heat (including radiation) and mass transport through correlations with ad hoc parameters based on experimental studies. With this model, we correctly predicted the profiles along the reactor for all species. Only CO_2 had a relevant relative error, but its composition was very low. The solid temperature was well reproduced as well, whereas the gas temperature was somewhere higher than the experimental temperature, possibly due to overestimation of the heat transport coefficient. Analysis of the transport limitations found that O_2 and H_2O had large concentration gradients between gas and surface due to their involvement in the total oxidation, which is a very fast reaction. The analysis thus demonstrated that production and consumption rates at the catalytic surface were frequently sufficiently high so as to enter a diffusive regime. Accordingly, we highlight the need to augment the implementation of detailed surface chemistry with some accounting of the transport processes of both mass and heat. In addition, we show that the Chilton–Colburn analogy can be seriously misleading under these conditions of locally fast heterogeneous kinetics.

1. Introduction

Partial oxidation of methane (POM) in monolithic reactors is competitive in converting natural gas into syngas, an intermediate for the syntheses of higher hydrocarbons and methanol:

$$CH_4 + (1/2)O_2 \rightarrow CO + 2H_2, \quad \Delta H_r^0 = -36 \text{ kJ mol}^{-1}. \tag{1}$$

A millisecond contact time reactor reaches this aim with unquestioned benefits. Noble metal catalysts lead to high performance in small volume and with little metal loading. Because of lower operating temperatures, NOx formation does not occur as in flame-based methane conversion. Among the three possible geometries—straight channel monolith, packed bed, and foam—the latter showed the high porosity typical of the first (causing low pressure drop) and the good radial mixing of the second, which improves the transport efficiency. Although this geometry has been widely tested through experiments, it remains a difficult challenge for modeling.

The single channel cannot be modeled in its actual shape. The low porosity of this foam makes it very dense, and thus the cubic-cell assumption, as in Ref. [10], does not apply. Thus, unless we adopt oversimplified assumptions on the geometry, the CFD cannot be used. Furthermore, for this system, gas-phase reactions are negligible at atmospheric pressure and become important only above 5 bar [8,14,31]. Because the low-pressure POM reaction occurs predominantly on the surface, a lumped model, based on empirical correlations, can be adopted [28] to find the transport coefficients, which applies regardless of the geometry.

The transport coefficients approach, coupled with a PFR model, has been used in many previous studies on catalytic combustion. A remarkable example, given in [25], used this approach to model the foam, honeycomb monolith, and packed-bed using Langmuir–Hinshelwood–Hougen–Watson kinetics. The interplay between chemical and physical processes has been high-

* Corresponding author. Fax: +39 049 827 5461.
E-mail addresses: daniela.dallenogare@unipd.it (D. Dalle Nogare), paolo.canu@unipd.it (P. Canu), schmi001@umn.edu (L.D. Schmidt).

0021-9517/$ – see front matter
doi:10.1016/j.jcat.2008.06.006

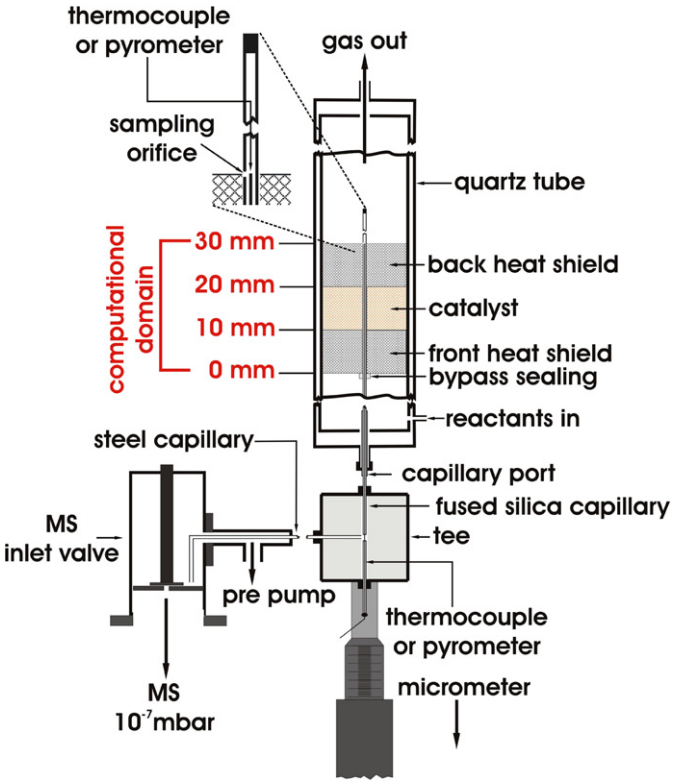

Fig. 1. Reactor setup and capillary sampling system. The computational domain is also sketched.

lighted in several previous studies as an essential issue in modeling (e.g. [22]), although a fundamental accounting for heat and mass transport requires CFD capabilities [5]. Following two preliminary studies investigating the relative weight of transport limitations over the conversion [2,3], a study using detailed surface kinetics was carried out [4] in which both heat and mass transfer coefficients were adopted, using an equivalent first-order kinetic constant to find an overall source term for each species that accounts for reaction and diffusion in series. A third example of such a model applied to POM was given in [30], in which a triangular channel monolith was modeled. Here the authors were interested mainly in describing the reactor startup. They also implemented the thermodynamic and transport coefficients, as well as the kinetics.

In the present work, we aimed to be more flexible regarding the parameter calculations. Using a kinetic interpreter makes the model easy to apply to any reaction system without the need for further programming. The model needs only be adjusted for the geometry and the boundary conditions, because the chemistry is handled in a very flexible way. From this model, we can extract kinetics information that can provide more insight into the relative importance of transport phenomena and reaction. In addition, the model provides information on surface coverage, which is difficult to measure.

2. Experimental

An extensive presentation of the experimental setup used to obtain the spatial data has been given previously [18–21]. A sketch of the setup, also illustrating the computational domain, is shown in Fig. 1.

The actual data set used in this work, taken from [7], comprised the spatial profiles of POM at steady state, including the concentration of the main gas species and both gas and surface temperatures. The reactor was adiabatic and autothermal, after a startup involving preheating up to the light-off temperature. Given the inlet composition and temperature of the feed, there were no more degrees of freedom, and the system evolved according to mass and energy conservation laws. Thus, a single data set was available for each inlet composition. The data presented are for a carbon-to-oxygen ratio of 1. The total flow rate was 5 $\mathrm{l\,m^{-1}}$ at room temperature and atmospheric pressure. The feedstock molar composition was 15.3% O_2, 29.1% CH_4, and 55.6% Ar. The reactor setup comprised three α-Al_2O_3 foam monoliths, the geometries of which are defined in Table 1. The first and third foam monoliths in the stack served as heat shields; the middle foam monolith was the catalyst loaded with 6 wt% Rh, without a wash coat.

Table 1
Geometric properties of the foam monolith

Property	Value
Foam material	α-Al_2O_3
Foam type	80 ppi
Pore diameter (d_{pore})	0.5 mm
Porosity (ε)	0.53
Surface to void volume ratio (S_V)	8000 $\mathrm{m^{-1}}$
Monoliths length (L)	10.0 mm
Monoliths diameter (D)	16.5 mm
Tortuosity factor (f)	0.6
Extinction coefficient (K)	2550 $\mathrm{m^{-1}}$

The composition profiles of the CH_4, CO, CO_2, H_2, and O_2 species were measured using a capillary technique [18]. The H_2O profile was not measured, but rather was obtained from the H and O balances using a mean squared error technique. Because the continuity equation could be applied to each atomic species, the lack of H in each point could be addressed to the H_2O molecule, as well as the lack of O. This led to two distinct numbers; the estimation was obtained minimizing the difference (squared) between each of those values and the estimation itself. Fig. 2 shows the catalyst profiles, extended 1 mm into the upstream and downstream heat shields and remaining constant elsewhere. The plot shows the catalyst inlet and outlet as well. CH_4 and O_2 reacted to produce CO, CO_2, H_2, and H_2O. The H_2O profile passed through a maximum and then decreased, consumed by the steam-reforming (SR) reaction:

$$\mathrm{CH_4 + H_2O = CO + 3H_2}, \quad \Delta H_r^0 = +206\ \mathrm{kJ\,mol^{-1}}. \tag{2}$$

CO_2 reforming seemed to be negligible on the Rh catalyst, because no maximum was evident in its profile:

$$\mathrm{CH_4 + CO_2 = 2H_2 + 2CO}, \quad \Delta H_r^0 = +247\ \mathrm{kJ\,mol^{-1}}. \tag{3}$$

CH_4 conversion was 80% at the catalyst exit, after reacting first with oxygen and then with water. CO_2 formed only in the presence of a large amount of oxygen. H_2 and CO increased monotonically, up to a final molar ratio of about 2, as in the POM.

The methane consumption rate was faster in the first half of the reactor and much slower in the rest of the reactor. This may be due to the decreasing reactant concentration, to the thermodynamic equilibrium approach used, or to lower temperatures. The system did not reach equilibrium, although it closely approached it. Table 2 compares the equilibrium results and experimental data at the reactor outlet. Thermodynamics predicted a higher methane conversion, achieved through the still-active endothermic SR reaction, at a lower temperature. CH_4 and H_2O should be lower than the values in the experimental products, with higher amounts of H_2 and CO. In terms of the composition paths, equilibrium likely would be reached with a longer catalytic monolith (i.e., higher contact time).

In our system, a thermocouple measured the bulk gas temperature, whereas a pyrometer measured the catalyst surface temperature (Fig. 3). Depending on the relative direction of the flow with respect to the pyrometer movement, two slightly shifted surface

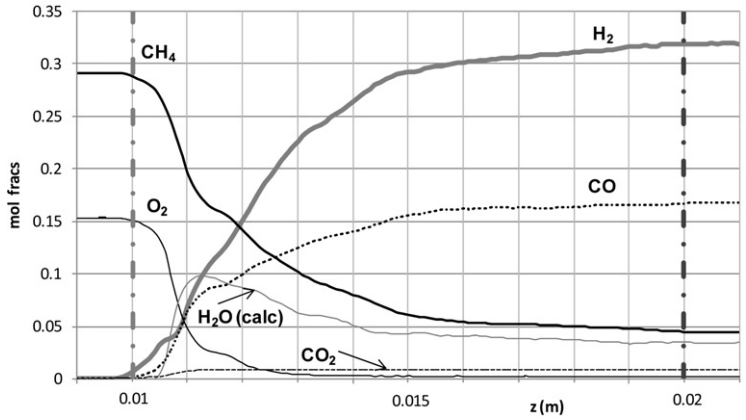

Fig. 2. Spatial profiles of experimental composition (H_2O is a calculated profile). Boundaries of the catalytic foam are shown.

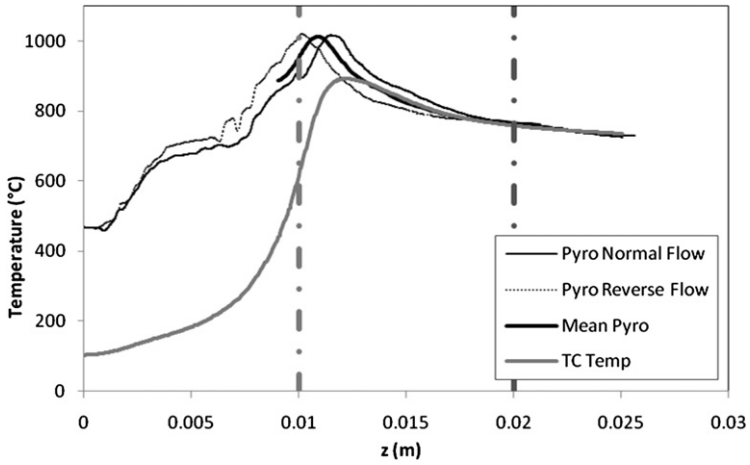

Fig. 3. Spatial profiles of experimental temperature.

Table 2
Adiabatic equilibrium results and absolute difference between equilibrium and experimental data

Property	Equilibrium	Experiments	Abs. diff.
Temperature	700 °C	758 °C	+58 °C
CH_4 conversion	87%	80%	−7%
Mole fractions:			
H_2	0.352	0.319	−0.033
O_2	0.000	0.002	+0.002
H_2O	0.022	0.036	+0.014
CH_4	0.028	0.045	+0.017
CO	0.170	0.167	−0.003
CO_2	0.017	0.009	−0.008

temperature profiles were obtained, showing the same maximum value but at different positions, possibly related to the viewing range of the fiberoptic probe. The reverse-flow curve refers to the gas flowing from bottom to top; the normal-flow curve, to the gas flowing from top to bottom. We averaged the two measurements to obtain a profile for comparison with the simulations.

The feed mixture entered the front heat shield (FHS) at about 100 °C. At the same position, the solid was at about 450 °C, due to the combination of solid conduction and heat transport toward the gas. The radiation leaving the face of the FHS was negligible, given the low surface temperature. The gas was heated and entered the catalytic section at 600 °C; the temperature difference of about 300 °C between the gas and the solid indicates a heat transport limitation. Both temperature profiles increased strongly in the first few millimeters inside the catalyst (due to the oxidation reactions), passed through a maximum, and then decreased less strongly, indicating that some endothermic (slower) reactions were occurring. The two profiles approached each other at the end of the reactor as heat production or consumption by surface reactions slowed. The maximum temperature read by the pyrometer was 1010 °C, and the gas exited the catalytic section at 760 °C.

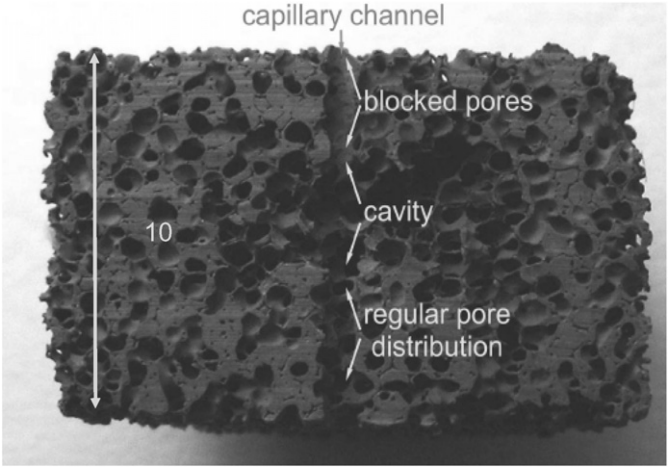

Fig. 4. Example of pore structure: an uneven distribution of pores produces a fine structure in the spatial profiles.

Fig. 4 shows a cross-section of an 80-ppi foam monolith, clearly indicating an irregular pore distribution. The fine structure in the species and the temperature profiles (Figs. 2 and 3) were likely

related to blocked pores and cavities along the scanning line of the capillary and should be disregarded.

Blocked pores also explain the delayed reactant conversion shown in Fig. 2. Both methane and oxygen conversion were low in the first 0.5 mm of the catalytic monolith and then decreased rapidly after that, with a more likely exponential decay. Generally, uniform inlet velocity and good radial mixing help ensure that the presence of the capillary does not interfere with the reaction, so that the measured composition is representative of the entire cross-section at that axial position. Nevertheless, if the capillary faces blocked pores, then radial mixing is hampered, and reactant conversion slows. The finding that the delay in the conversion of CH_4 and O_2 had the same extension as a single pore diameter (0.5 mm) supports this interpretation.

Although new reactor configurations allow 2–3D inspection of the catalysts [1,9], it is common practice to investigate exit composition. Nonetheless, having information along the reactor may aid the kinetic characterization. The spatial profiles allow validation of the modeling of this reaction system in much more detail.

3. Model equations

3.1. An ideal model: the PFR

The plug-flow reactor (PFR) is the simplest model that can be written for a system in flow. It states that convection of species, as well as of heat, is equal to its production/consumption on the catalytic surface. No homogeneous reactions are accounted for, because they are not significant at atmospheric pressure [8,14,31]. With surface chemistry, the production rate is written on a surface basis. Thus the production, in terms of both mass and in energy balances, must be multiplied by the surface-to-volume ratio, S_V, to make these terms on a volume basis.

Physically, this model assumes infinite radial mixing with no transport resistance, which results in a flat profile, and zero axial mixing. This means that a segregated volume of fluid flows through the channel with no exchanges with adjacent fluid elements. The mathematical formalization of this model is as follows:

$$\text{PFR MB:}\quad \rho v\frac{d\mathbf{Y}}{dz} = S_V\dot{\mathbf{s}}\cdot\mathbf{W},\quad Nsp = 7, \tag{4}$$

$$\text{PFR EB:}\quad \rho v c_P\frac{dT}{dz} = S_V\left(\sum_{k=1}^{Nsp} h_k\dot{s}_k\right). \tag{5}$$

This system of equations is closed due to the ideal gas law, which relates density to composition and temperature: $\rho = \rho(Y, T)$.

This model is well applicable to systems with homogeneous flow kinetics and $Pe \gg 1$ (axial diffusion can be neglected). With heterogeneous kinetics, it is valid only when chemistry is the controlling regime compared with transport.

3.2. The model including the transport phenomena

The reactor model that includes transport phenomena consists of transient, one-dimensional balances for heat and species. The reactor is represented as a straight channel with a constant cross-section, where the bulk gas phase has certain composition and properties, with a thin layer of gas close to the solid surface with its own composition and properties. Using conventional terminology, we designated these quantities the boundary layer (BL). In what follows, we call this model the foam model for simplicity. The following equations are written on a void volume basis:

$$\text{Bulk MB:}\quad \rho_G\frac{\partial\mathbf{Y_G}}{\partial t} = -\rho_G\mathbf{v}\frac{\partial\mathbf{Y_G}}{\partial z} + \rho_G D\frac{\partial^2\mathbf{Y_G}}{\partial z^2} - \rho_G S_V\mathbf{K_C}(\mathbf{Y_G} - \mathbf{Y_{BL}}),\quad Nsp = 7, \tag{6}$$

$$\text{BL MB:}\quad \rho_{BL}\frac{\partial\mathbf{Y_{BL}}}{\partial t} = \rho_{BL}S_V\mathbf{K_C}(\mathbf{Y_G} - \mathbf{Y_{BL}}) + S_V\dot{\mathbf{s}}\cdot\mathbf{W},\quad Nsp = 7, \tag{7}$$

$$\text{Bulk EB:}\quad \rho_G\mathbf{c}_P\frac{\partial T_G}{\partial t} = -\rho_G\mathbf{v}\mathbf{c}_P\frac{\partial T_G}{\partial z} + \lambda_G\frac{\partial^2 T_G}{\partial z^2} - S_V K_T(T_G - T_S), \tag{8}$$

$$\text{Solid EB:}\quad \frac{1-\varepsilon}{\varepsilon}\rho_S c_{P,S}\frac{\partial T_S}{\partial t} = \frac{1-\varepsilon}{\varepsilon}f\frac{\partial}{\partial z}\left(\lambda_S\frac{\partial T_S}{\partial z}\right) + S_V K_T(T_G - T_S) - S_V\left(\sum_{k=1}^{Nsp} h_k\dot{s}_k\right) - S_V\sigma\left(T_S^4 - \frac{K}{2}\int_{-\infty}^{+\infty} T_S^4(z+z^*)e^{-K|z^*|}\,dz^*\right). \tag{9}$$

The ideal gas law completes the model. All thermodynamic and transport properties of the gas were estimated as functions of temperature and composition, by means of a kinetic interpreter that uses the GRImech3.0 database [15]. The bulk MB contains the terms of accumulation, axial convection, and diffusion and flux from the bulk to the surface for the stable gas species H_2, O_2, H_2O, CH_4, CO, CO_2, and Ar. In the BL MB accumulation equals the flux from the bulk to the surface plus the production or consumption at the catalytic surface. Transient balances were written to simplify the solution, not to effectively model dynamics, provided that measurements were obtained at steady state. At steady state, each accumulation term goes to zero; in addition, from the continuity equation, we obtain $\rho v = \text{const}$. It can be proven that the time scale of the first three equations is much lower than the energy accumulation in the solid, so that the system goes through pseudo-steady states for composition and gas temperature compared with changes in the solid temperature, T_S. This simplifies the simulations considerably. Because we are interested only in the steady-state solution, the heat capacity of the solid may be decreased from its original value of about 1200 $\mathrm{J\,kg^{-1}\,K^{-1}}$ (because it is a convergence parameter), thereby decreasing the time to reach the steady state.

The bulk EB is analogous to the bulk MB containing accumulation, axial convection, and conduction and the heat flux from the bulk to the solid. In the solid EB, the accumulation and conduction terms must be written on a solid volume basis. For this reason, they must be divided by the void volume and multiplied by the solid volume, introducing the term $(1-\varepsilon)/\varepsilon$. Because the solid structure of the monolith has a discontinuous nature, the heat conduction in the axial direction encounters high resistance (through a tortuosity factor). At high temperature, however, the presence of pores is no longer an obstacle to the heat transport, which can now occur by radiation. Thus, the equation contains a radiation term, which becomes important in the catalyst region, where the surface temperature exceeds 1000 °C. Radiation is transferred from one pore face to the others, and the amount of radiation absorbed by the gas can be neglected. Heat transfer by radiation becomes very important at high temperatures as the emitted power increases with the 4th power of the temperature.

Pe numbers must be evaluated to determine whether or not to include axial mass diffusion and temperature conduction in the gas phase in the model. For the temperature, Pe_T reaches unity at the highest temperatures. For $Re < 5$, the dispersion coefficient is very close to the molecular diffusion [24]; thus we use the latter to calculate Pe_M. For H_2 Pe_M is close to unity, even a little lower, whereas it is >1 for the other species (meaning that convection is more important for them). Consequently, the contributions of gas heat conduction and diffusion must be included in the model.

3.3. Boundary conditions

Because the model contains second-order differential equations, the system must be solved as a boundary value problem (BVP). This section presents the boundary conditions.

3.3.1. Front heat shield (FHS) inlet ($z = 0$)

The gas temperature and composition are those in the feed. These result in $Nsp + 1$ Dirichlet boundary conditions,

$$\mathbf{Y}_G = \mathbf{Y}_{G,\text{feed}} \quad \text{and} \quad T_G = T_{G,\text{feed}}.$$

The gas diffusivity is assumed to be zero, because no concentration gradients are expected 1 cm from the catalyst and, in the presence of a heat shield and the relatively low temperatures, no radiation leaves the reactor. The following $Nsp + 1$ Neumann boundary conditions also apply:

$$\left.\frac{\partial \mathbf{Y}_G}{\partial z}\right|_{z=0} = 0 \quad \text{and} \quad \left.\frac{\partial T_S}{\partial z}\right|_{z=0} = 0.$$

3.3.2. Back heat shield (BHS) outlet ($z = 0.03$ m)

At the exit, we neglect the radiation leaving the BHS, obtaining a zero gradient condition for the solid temperature profile. This assumption is justified because the heat losses by radiation at the BHS are <5% of the total amount released by the reaction. Furthermore, because the gas and solid temperatures approach each other at the end of the BHS, the gas temperature gradient is negligible, and there is no conduction in the gas at the exit. Even if redundant, the gas zero diffusivity also is set at the exit, because it is physically reasonable and numerically stable. Therefore, $Nsp + 2$ Neumann boundary conditions apply at the exit of the BHS:

$$\left.\frac{\partial \mathbf{Y}_G}{\partial z}\right|_{z=0.03\ \text{m}} = 0, \quad \left.\frac{\partial T_G}{\partial z}\right|_{z=0.03\ \text{m}} = 0 \quad \text{and} \quad \left.\frac{\partial T_S}{\partial z}\right|_{z=0.03\ \text{m}} = 0.$$

3.3.3. Initial guess ($t = 0$)

The system startup is simulated in the same way as is done in the laboratory. Starting from a cold reactor with the feed gas flowing, the central catalytic monolith is heated up to the catalyst's light-off temperature. After reaction light-off, the heater is switched off, and the reactor operates autothermally, approaching steady state. A change in the operating conditions (e.g., switching from one composition to another) starts from the previous steady state, a physical state of the system, and moves to another steady state. Interestingly, the dynamic model allows predicting conditions (e.g., preheating temperature) for self-sustainability of the reactor.

3.4. Equation parameters

As in Ref. [19], the solid component of the foam was considered polycrystalline alpha-alumina, the intrinsic thermal conductivity of which was obtained from the literature [16] and included in the model as a polynomial function of temperature. Because the nominal characteristics of the 80-ppi foam were not suitable for describing our monolith, pore diameter and porosity were measured with image analysis, as was the extinction coefficient [7]. The tortuosity factor was obtained from the literature [10].

Transport coefficient correlations for foams of our pore size are not available in the literature. Other formulas [12], extrapolated from their validity range, turned out to overestimate transport. Our reactor characterization revealed that the temperature profiles calculated with such correlations were too close to one another to represent the actual operation of the reactor. This behavior also is in agreement with the findings of previous works [23,27], in which *Re* was also kept below the validity of standard theories based on transport around a sphere or in a single cylinder. The authors found that for $Re < 10$, correlations for heat and mass transfer should have a *Re* exponent >0.5, which is suitable only for higher Reynolds numbers.

Experiments were carried out with a model reaction (CO oxidation), at adiabatic conditions and with a CO lean mixture, which is a well-established benchmark [11]. Details of our measurements have been given previously [7]. The correlations that we obtained for our 80-ppi foam, in which the characteristic length used in dimensionless numbers is the inverse of the geometric surface to total bed (thus, not the void) volume, $1/S'_V$, are expressed by

$$Sh' = 0.0483 Re'^{0.753} Sc^{1/3}, \tag{10}$$

$$Nu' = 0.0483 Re'^{0.753} Pr^{1/3}. \tag{11}$$

All numbers marked with a prime are based on the total bed volume.

3.5. Microkinetic model

The microkinetic model for CH_4 oxidation on Rh was initially developed by Schmidt et al. [17] and subsequently improved by others [29] to a final 38-step surface mechanism involving 7 gas species and 12 surface species (Table 3). It contains adsorption and desorption reactions, as well as the proper surface reactions. Because the kinetic model was developed on a 3 wt% Rh loading (half the amount used in the present work), the surface-to-volume ratio was doubled in the production terms.

4. Numerical resolution

Although we need to solve a steady-state problem, the use of transient equations simplifies the solution and closely follows the physics. An analogous model, written for a steady-state problem, is an algebraic differential equation (ADE) system, which includes a second-order differential equation requiring solution of a BVP. Instead, we preferred to solve the full transient of the process, which is now described by an ordinary differential equation system in time, from a known physical state of the reactor up to the steady state. This procedure leads to a much sparser Jacobian matrix, and the ordinary differential equation system is extremely stable.

The derivatives were discretized with respect to a nonuniform spatial grid of 130 elements spanning the three foam pieces. The mesh was finer where the gradients were steeper, at the entrance and the exit of the FHS, and at the catalyst entrance. The FHS was divided in 45 steps and the catalyst in 60 steps, whereas the BHS had a uniform mesh of 25 steps. Four-step Lagrange polynomials were used to approximate the first and second derivatives. A three-step Lagrange polynomial (simpler than the four-step ones because it does not have to be derived, but can be integrated) was substituted in the T_S^4 inside the integral, so that the integral itself was calculated analytically. The resulting formulas were introduced in the algorithm, making it more efficient than the numerical integration.

The analytic result of the integral was

$$\begin{aligned}\frac{K}{2}\int_{-\infty}^{+\infty} T_S^4(z+z^*)\cdot e^{-K|z^*|}\,dz^* &= \frac{1}{K^2}\left[\frac{2\cdot T_S^4(x_1)}{(x_1-x_2)(x_1-x_3)} + T_S^4(x_2)\cdot\left(\frac{2}{(x_2-x_1)(x_2-x_3)} + K^2\right)\right.\\ &\quad \left. + \frac{2\cdot T_S^4(x_3)}{(x_3-x_1)(x_3-x_2)}\right].\end{aligned} \tag{12}$$

The chemistry was determined using the free Cantera software [13]. Cantera is used in Matlab [26] routines that can be easily coupled with the main Matlab program to give thermodynamic and

Table 3
Surface reaction mechanism

	A (cm, mol, s)	E_a (kJ mol^{-1})
1. Adsorption		
$H_2 + Rh(s) + Rh(s) \rightarrow H(s) + H(s)$	1.000×10^{-02}	s.c.[a]
$O_2 + Rh(s) + Rh(s) \rightarrow O(s) + O(s)$	1.000×10^{-02}	s.c.[a]
$CH_4 + Rh(s) \rightarrow CH_4(s)$	8.000×10^{-03}	s.c.[a]
$H_2O + Rh(s) \rightarrow H_2O(s)$	1.000×10^{-01}	s.c.[a]
$CO_2 + Rh(s) \rightarrow CO_2(s)$	1.000×10^{-05}	s.c.[a]
$CO + Rh(s) \rightarrow CO(s)$	5.000×10^{-01}	s.c.[a]
2. Desorption		
$H(s) + H(s) \rightarrow Rh(s) + Rh(s) + H_2$	$3.000 \times 10^{+21}$	77.8
$O(s) + O(s) \rightarrow Rh(s) + Rh(s) + O_2$	$1.300 \times 10^{+22}$	$355.2–280\theta_{O(s)}$
$H_2O(s) \rightarrow H_2O + Rh(s)$	$3.000 \times 10^{+13}$	45.0
$CO(s) \rightarrow CO + Rh(s)$	$3.500 \times 10^{+13}$	$133.4–15\theta_{CO(s)}$
$CO_2(s) \rightarrow CO_2 + Rh(s)$	$1.000 \times 10^{+13}$	21.7
$CH_4(s) \rightarrow CH_4 + Rh(s)$	$1.000 \times 10^{+13}$	25.1
3. Surface reactions		
$H(s) + O(s) \rightarrow OH(s) + Rh(s)$	$5.000 \times 10^{+22}$	83.7
$OH(s) + Rh(s) \rightarrow H(s) + O(s)$	$3.000 \times 10^{+20}$	37.7
$H(s) + OH(s) \rightarrow H_2O(s) + Rh(s)$	$3.000 \times 10^{+20}$	33.5
$H_2O(s) + Rh(s) \rightarrow H(s) + OH(s)$	$5.000 \times 10^{+22}$	104.7
$OH(s) + OH(s) \rightarrow H_2O(s) + O(s)$	$3.000 \times 10^{+21}$	100.8
$H_2O(s) + O(s) \rightarrow OH(s) + OH(s)$	$3.000 \times 10^{+21}$	171.8
$C(s) + O(s) \rightarrow CO(s) + Rh(s)$	$3.000 \times 10^{+22}$	97.9
$CO(s) + Rh(s) \rightarrow C(s) + O(s)$	$2.500 \times 10^{+21}$	169.0
$CO(s) + O(s) \rightarrow CO_2(s) + Rh(s)$	$1.400 \times 10^{+20}$	121.6
$CO_2(s) + Rh(s) \rightarrow CO(s) + O(s)$	$3.000 \times 10^{+21}$	115.3
$CH_4(s) + Rh(s) \rightarrow CH_3(s) + H(s)$	$3.700 \times 10^{+21}$	61.0
$CH_3(s) + H(s) \rightarrow CH_4(s) + Rh(s)$	$3.700 \times 10^{+21}$	51.0
$CH_3(s) + Rh(s) \rightarrow CH_2(s) + H(s)$	$3.700 \times 10^{+24}$	103.0
$CH_2(s) + H(s) \rightarrow CH_3(s) + Rh(s)$	$3.700 \times 10^{+21}$	44.0
$CH_2(s) + Rh(s) \rightarrow CH(s) + H(s)$	$3.700 \times 10^{+24}$	100.0
$CH(s) + H(s) \rightarrow CH_2(s) + Rh(s)$	$3.700 \times 10^{+21}$	68.0
$CH(s) + Rh(s) \rightarrow C(s) + H(s)$	$3.700 \times 10^{+21}$	21.0
$C(s) + H(s) \rightarrow CH(s) + Rh(s)$	$3.700 \times 10^{+21}$	172.8
$CH_4(s) + O(s) \rightarrow CH_3(s) + OH(s)$	$1.700 \times 10^{+24}$	80.3
$CH_3(s) + OH(s) \rightarrow CH_4(s) + O(s)$	$3.700 \times 10^{+21}$	24.3
$CH_3(s) + O(s) \rightarrow CH_2(s) + OH(s)$	$3.700 \times 10^{+24}$	120.3
$CH_2(s) + OH(s) \rightarrow CH_3(s) + O(s)$	$3.700 \times 10^{+21}$	15.1
$CH_2(s) + O(s) \rightarrow CH(s) + OH(s)$	$3.700 \times 10^{+24}$	158.4
$CH(s) + OH(s) \rightarrow CH_2(s) + O(s)$	$3.700 \times 10^{+21}$	36.8
$CH(s) + O(s) \rightarrow C(s) + OH(s)$	$3.700 \times 10^{+21}$	30.1
$C(s) + OH(s) \rightarrow CH(s) + O(s)$	$3.700 \times 10^{+21}$	145.5

[a] Value sticking coefficient. Surface site density: $\Gamma = 2.72 \times 10^{-9}$ mol cm^{-2}.

transport properties and to calculate species production rates. It allows mechanisms to be handled in the Chemkin format, the most common way to publish and distribute microkinetic models consisting of elementary steps. It also supports the typical features of surface mechanisms, including coverage dependences, sticking coefficients, and so on. Equilibrium was calculated using the Cantera "equilibrate" routine.

5. Results and discussion

5.1. Predictions by a simpler model, the PFR

With the aim of gaining insight into the interplay between surface chemistry and transport phenomena, a simple PFR calculation is helpful because it neglects transport by definition. The PFR model is an ideal reactor model, in which at each axial position, axial convection equals production and no transport resistance of any kind interferes with the kinetics. Because the heat model needed to describe this reactor setup is rather complicated and may lead to some uncertainties, we use the experimental surface temperature for the PFR calculations, thereby avoiding the solution of a heat balance. This reveals the effect of ignoring mass transport resistances in mass balances.

Fig. 5 shows profiles of the four species CH_4, CO, O_2 and H_2 compared with the experimental data. Comparing the exit compositions shows that the model's predictions are very good for all species, with a CH_4 conversion of 82%, only 2 points higher than measured. Nonetheless, the experimental exit composition is close to equilibrium, and any reactor model with arbitrary kinetics will result in similar good agreement as long as equilibrium is predicted correctly.

In the literature, model validation based on one point reactor exit data is common, easily leading to misinterpretation if equilibrium is approached as closely as in the present case. Spatial profiles, on the other hand, are a much more stringent model validation. Fig. 5 shows that the PFR model clearly overestimates reactant consumption and product formation at the catalyst entrance, because it does not consider transport resistance; for example, the probe detects the presence of oxygen up to 3–4 mm inside the catalyst, whereas the PFR model predicts total consumption of O_2 within 0.5 mm.

In general, discrepancies indicate that consumption/production of all of the species at the catalyst entrance is diffusion-limited (i.e., the reaction is much faster than diffusion). In other words, the composition near the surface differs from that in the bulk of the gas. To properly describe the reaction system, the actual production rate at the surface must be calculated using the concentration at the surface. The finding that a diffusion regime prevails in a significant part of the foam demonstrates that the PFR model is not a suitable reactor model.

5.2. Results from the foam model

Fig. 6 shows results from the foam model compared with the experimental data. Compared with the PFR model, the foam model including transport describes the experimental profiles much better. The slight differences in the first 0.5 mm are, as discussed earlier, experimental artifacts caused by a blocked pore at the catalyst entrance. This pore blocking masks the actual composition by suppressing radial mixing. Note that the composition profiles approach the experimental profiles after 1 mm, which corresponds to two pore diameters, and the predicted composition more closely matches the experimental data along the reactor. This finding supports the hypothesis that only the pore structure impedes some sort of exponential profile to setup. The slopes are close to the experimental curves, and each species' final composition has <0.01 absolute error in the mole fraction. In Fig. 6, the adopted mesh around the catalyst section is identified by the markers in the simulated curves.

Fig. 6a shows the predicted mole fractions of O_2, CH_4, and H_2. Because methane and oxygen underwent some axial diffusion, their concentration was slightly lower at the catalyst inlet than in the feed. Inside the catalyst, their decay was exponential, as expected.

Moreover, the simulated H_2 profile increased more rapidly at the catalyst entrance than in the experimental profile, but its high back-diffusivity partly compensated for the delay due to the pore blockage, and the deviations were not as pronounced as for the heavier species. Indeed, the curve of H_2 exhibited the earliest variation of the 6 species studied in both the experimental and calculated profiles. The predicted CH_4 conversion and H_2 production at the reactor exit were only slightly lower than the measured values.

Fig. 6b shows the other gas species, H_2O, CO, and CO_2. Here again, a 0.5-mm delay occurred at the catalyst entrance. The exit CO was lower than expected, obviously not because CH_4 conversion was underestimated, but rather because CO_2 formation was overpredicted. This could be due to several reasons, including some deficiency in the kinetic mechanism, an inadequacy of the transport coefficient approach, or a discrepancy between the calculated and experimental solid temperatures. Other possible reasons could

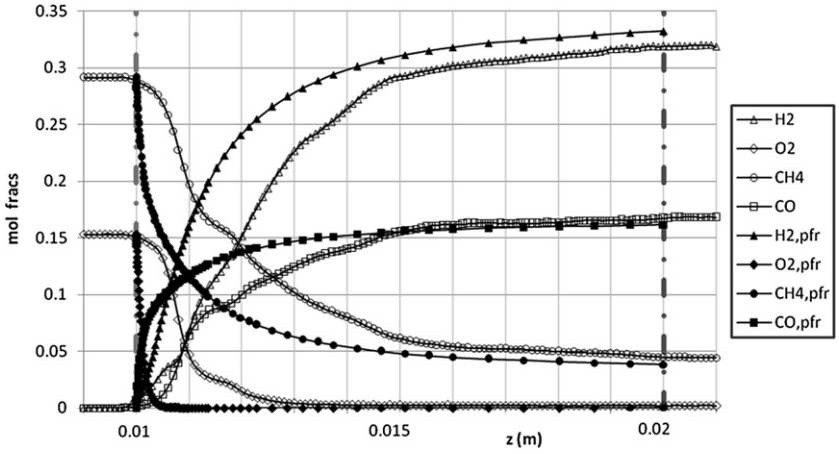

Fig. 5. Gas-phase composition along the reactor: calculated by a PFR model with the real surface temperature (filled symbols), and experimental measurements (empty symbols).

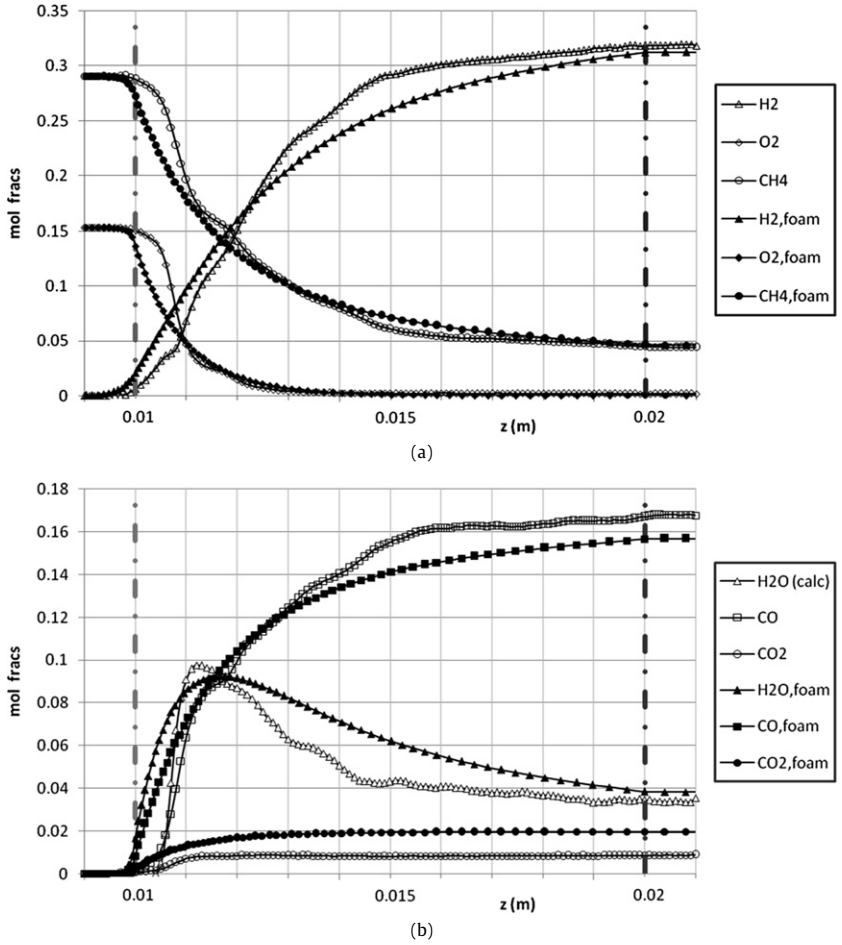

Fig. 6. Mole fractions of H_2, O_2 and CH_4 (a), and H_2O, CO and CO_2 (b) predicted by the "foam" model, compared with those experimental (experimental H_2O is calculated from the oxygen and hydrogen balances).

be ascribed to the irregularity of the foam structure, which might locally interfere with the availability of oxygen on the surface in oxidation of the carbon atoms. The available information is insufficient for determining the actual cause of this behavior.

Fig. 6b also gives the H_2O profile, showing that it goes through a maximum. H_2O switched from being a product to a reactant after the O_2 was completely consumed. Even more interestingly, CH_4 appeared to react in parallel with both O_2 and H_2O even when oxygen was still available.

Fig. 7 compares simulated and experimental temperature profiles. In the FHS, the T_S increased monotonically up to the value at the catalyst entrance. Heat transport by convection, axial conduction, radiation, and transport between the phases was responsible for the gas heating in the inward direction and the solid cooling in the outward direction. In the catalyst section, the heat of reaction kept the two temperatures T_S and T_G different. At the catalyst entrance, the strongly exothermic reactions made the solid hotter than the gas. After the oxygen was consumed, only endother-

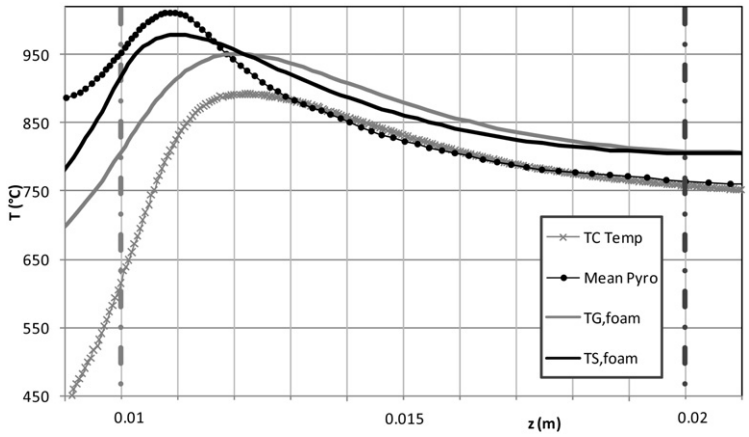

Fig. 7. Gas and surface temperature profiles predicted by the foam model, compared with the experimental. Catalytic foam boundaries are also reported.

mic reactions occurred on the solid; thus, the solid temperature dropped below the gas temperature, and heat transport occurred in the opposite direction. As long as chemical reactions occurred at the catalyst, heat transport limitations impeded the two phases from achieving the same temperature.

Up to the maximum, the calculated solid temperature was lower than that found experimentally. The maximum itself was predicted to be 30 °C lower; however, the position of the maximum was approximately the same as in the actual monolith, confirming the agreement of the chemistry but also indicating that the descriptions of solid conduction and radiation heat transfer were consistent with the actual physics. This justifies using the mean pyrometer temperature profile instead of the normal or reverse ones. Indeed, the composition profiles are predicted with high accuracy, so the enthalpy of reaction is reliable, and the position of the maximum is trustworthy (although not its absolute value, which depends on many transport features). This position corresponds to that of the mean temperature profile, providing evidence in favor of this choice.

If the maximum solid temperature is determined by a switch from an exothermic reaction to an endothermic reaction, then the maximum in the gas temperature is governed only by heat transport from and to the solid. No heat production or consumption occurs in the bulk gas phase. The position of the maximum in the gas temperature is properly predicted, but now the value is higher than the experimental. The interplay between heat transport limitation and convection in the gas-phase results in the maximum in the gas temperature being located downstream from that in the solid. In the calculated profiles, the gas temperature maximum occurred exactly where the two temperatures crossed. This must be so because in the steady state, the accumulation term of Eq. (8) was zero, the interphase heat transport was zero (because there was no temperature difference between the two phases), and gas conduction played a minor role in the heat transport (because the gradients were low around the maximum). Thus, the convection term was almost zero, meaning that the temperature gradient was nearly zero, and the temperature profile passed through a maximum. The experimental temperature profiles crossed far away from the location of the experimental T_G maximum, casting some doubt on the accuracy of the experimental measurements. Agreement of the experimental and calculated surface temperatures is more important for validating the surface chemistry mechanism, however.

The model predicted a 50 °C higher solid temperature at the catalyst exit compared with the experimental value. This discrepancy may be due in part to the adiabatic assumption, which implies no heat losses, but more likely results from overprediction of CO_2 formation, which liberates more heat than CO formation. The gas temperature generally was overestimated all along the reactor, in part because the transfer coefficients were derived for the mass transport and extended to the heat transport using the Chilton–Colburn analogy, which states that the basic mechanisms and mathematics of heat, mass, and momentum transport are essentially the same. However, as shown previously [6], this analogy is questionable in the presence of a fast reaction, when mass transfer coefficients are significantly greater.

In the BHS (not shown in Fig. 7), the two temperatures approached each other and remained constant, due to the lack of driving force for any heat exchange. The experimental profiles revealed a negative slope at the reactor exit due to some heat loss.

An integral heat balance was evaluated, comparing the enthalpy of the preheated feedstock with that of the products at the BHS exit conditions. The heat balance of the entire reactor dropped to about 1% error. The adiabatic assumption, carried out through the heat balances, was satisfied. Because these balances are conservative, we do not need to superimpose the adiabatic temperature at the T_G, with the Dirichlet-like boundary condition, at the exit: $T_{G,z=0.03\ m} = T_{G,adiab}$. Indeed, the Neumann-like boundary condition $(dT_G/dz)_{z=0.03\ m} = 0$, together with the conservation of energy, are sufficient to guarantee that the model is adiabatic.

5.3. Heat and mass transport limitations

Once the model was validated for gas composition and both gas and solid temperatures, it was used to speculate about those variables that could not be measured, including the gas species at the surface. Fig. 8a compares the reactant concentration in the bulk gas phase and over the catalyst surface. The O_2 concentration at the surface was close to zero over the entire oxidation zone, indicating full mass transport limitation. On the surface, the reactions consumed O_2 much faster than physical transport processes could provide it. The methane concentration at the surface also was noticeably lower than in the bulk gas phase, but the effect was much less than for oxygen.

Fig. 8b compares the concentrations of H_2 and CO in the boundary layer and in the gas phase. Both species were produced continuously, and their profiles increased monotonously. As expected, the rapid diffusion of H_2 resulted in a smaller difference between the bulk and the surface, whereas for CO, the difference was more pronounced, and a high mole fraction was present near the surface.

Fig. 8c compares CO_2 and H_2O using the same scale. To understand these curves, keep in mind that the BL composition refers to a thin layer of gas close to the surface, where the composition is the direct consequence of what is consumed and produced locally by the reaction. The high concentration of water in the BL at the

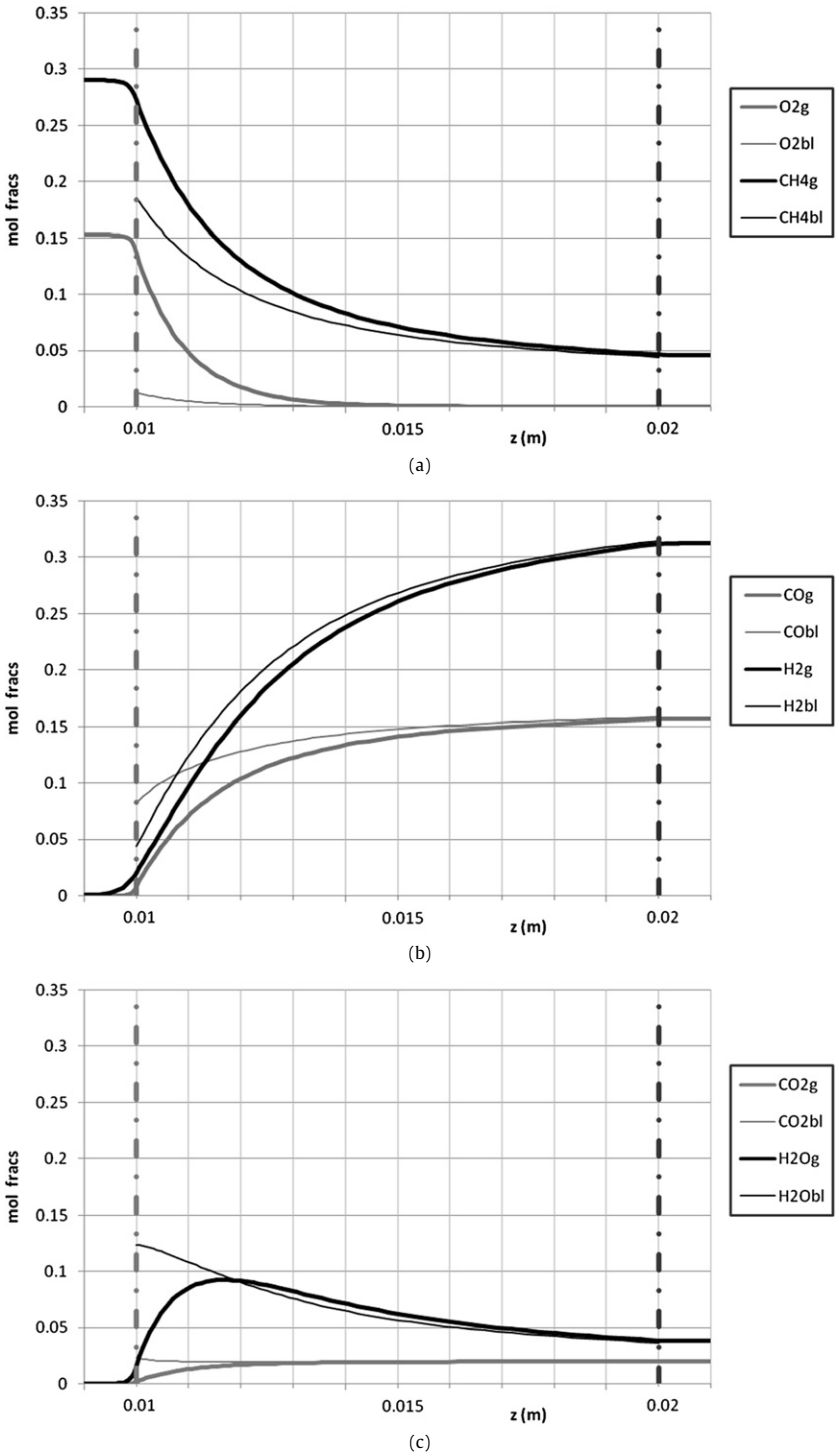

Fig. 8. Composition (mole fractions) in the bulk (thick lines) and at the catalytic surface (thinner lines) for the species: (a) O_2 and CH_4; (b) CO and H_2; (c) CO_2 and H_2O.

beginning, along with its negative slope, support the finding that CH_4 reacted in both oxidation and reforming reactions in parallel starting at the beginning of the reactor. Note that no maximum was seen in the boundary layer composition of H_2O; rather, the maximum production was seen at the entrance, where the oxygen concentration was highest. A crossing between the bulk and the boundary layer mole fraction was seen, meaning that water turned from product (when the $Y_{BL} > Y_G$) to reactant ($Y_{BL} < Y_G$). The reaction rates were much slower in the steam-reforming zone than in the oxidation zone, and the composition differences were lower in the former. Moreover, CO_2 had a relatively high mole fraction at the beginning, which decreased to reach the value of the bulk mole fraction after about 3 mm, the position at which O_2 was completely consumed close to the surface. After that position, the production rate of CO_2 was near zero, and no differences in the bulk and boundary layer compositions were seen.

The model also can provide information on surface coverages, which are not accessible experimentally. The kinetic mechanism includes 12 surface species: Rh(s), H(s), H_2O(s), OH(s), CO(s), CO_2(s), CH_4(s), CH_3(s), CH_2(s), CH(s), C(s), and O(s). Their compositions are given as site fractions, so that the total amount sums to unity. Fig. 9a shows coverages >1%. Due to mass transport lim-

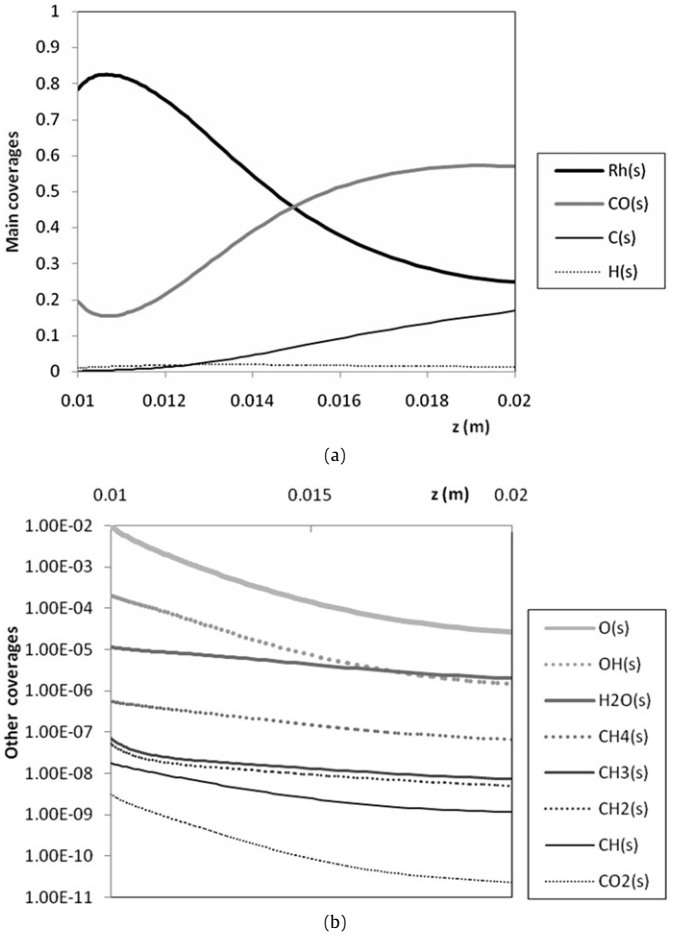

Fig. 9. (a) Surface coverages of the main surface species: Rh(s), CO(s), C(s), and H(s). (b) Surface coverages of other species, in semi-logarithmic plot.

itations and the high temperatures, >80% of the Rh sites in the oxidation zone were empty, compared with about 25% of the Rh sites at the exit. The fact that most catalytic sites were unused throughout the reactor decreased the sensitivity of the model for the accurate number of surface sites available. CO(s) was the most abundantly adsorbed species in the entire catalyst, with coverage of 0.15–0.57. The C(s) was next, increasing uniformly from nearly 0 to 0.17. H(s) never exceeded coverage of a few percent throughout the entire reactor.

Fig. 9b shows the coverages of the other surface species in a semilogarithmic plot. These coverages were very low, indicating that these species either were rapidly consumed by the reaction (intermediates) or desorbed very quickly (stable species). In particular, O(s) was <1% due to its high consumption rate, which exceeded the transport rate in the bulk. This strong oxygen deficit at the Rh surface is likely the main reason for the high selectivities to the partial oxidation products H_2 and CO.

From the boundary layer species balance (the BL MB), we obtain that the difference between the composition in the bulk and that in the boundary layer is proportional to the ratio of the production rate to the transport coefficient. Fig. 10 compares the quantities $\dot{s}$, K_C, and $\Delta X = |X_G - X_{BL}|$, all scaled to the values of CH_4, at the catalyst entrance. The mass transfer coefficient was directly related to the species diffusivity as $K_{C,i} \propto D_i^{2/3}$, according to the Sh' correlation used.

Note that CH_4 and O_2 exhibited comparable diffusivity, but O_2 reacts with a higher molecularity; thus $\Delta X_{O_2} \approx 1.5\Delta X_{CH_4}$. On the other hand, H_2 and CO_2 had the same composition difference, even when $K_{H_2} = 3K_{CO_2}$. This is because the hydrogen production rate was three times higher than the CO_2 production rate ($\dot{s}_{H_2} = 3\dot{s}_{CO_2}$); thus, the ratio $\dot{s}_i/K_{C,i}$ was the same.

Our findings confirm that the transport limitation depends on both the diffusivity and the reactivity of a species. The difference between gas and surface concentrations will be greater if a species has either low diffusivity or high reactivity. As mentioned previously, transport rates are very sensitive to the actual rate of reaction of a species. Based on our findings, we can draw two important conclusions: (i) A representative model must include bulk-surface transport of both heat and mass, and (ii) for reacting systems with fast heterogeneous kinetics [6], the Chilton–Colburn analogy must be used with care.

Using the model, we also could calculate the residence time inside different monolith sections, which depends on both the local temperature and the variation in moles due to the reaction. The results—6 ms in the FHS, 3 ms in the catalyst, and 3 ms in the BHS—clearly justify using the term "millisecond contact time reactor."

6. Conclusion

We used spatially resolved measurements of temperature and concentration to critically analyze the chemistry and transport limitations in the POM reaction carried out on Rh supported on a foam catalyst. Our analyses were based on a PFR model and a foam model, which shared a detailed surface chemistry but had different gas–surface transport processes. Experimental data include axial profiles of bulk concentration and of both gas and solid temperatures. The simulation with a PFR model predicted outlet concentrations very close to the measured ones, but only because model and experiment closely approached equilibrium. Significant disagreement between PFR predictions and measurements, particularly in the initial region, became evident as the profiles developed. This demonstrates the existence of regions in which strong diffusive limitations prevail, requiring an extension of the simple PFR model to account for transport limitations.

We developed a pseudo-1D model (the foam model) that differentiates the species and temperature in the bulk gas phase and at the surface and also describes heat and mass transport through correlations with parameters based on dedicated experiments. The solid heat balance contains both a solid conduction term and a term describing the radiation transmitted through the porous structure. Both mass and heat Peclet numbers are close to unity, which imposes to include in the model axial mass diffusion and temperature conduction in the gas phase.

The foam model was able to correctly predict slopes and values for all of the species studied except CO_2, the yield of which was significantly overpredicted. The solid temperature was closely reproduced, whereas the shape of the calculated gas temperature profiles agreed only qualitatively, but the absolute values were higher than the measured ones. We attribute the overestimated gas temperature to an overestimated heat transport coefficient. Some of the minor discrepancies also might be due to experimental artifacts that remain to be investigated.

Using the insights provided by the model, we analyzed the transport limitations and found that the O_2 concentration was very low everywhere near the surface, due to the rapid consumption of O_2 by oxidation reactions. H_2O concentrations were always very high close to the catalytic surface, as well as at the catalyst entrance; its slope suggests that the oxidation and reforming reactions occurred in parallel from the beginning. Analysis of the surface coverages revealed that most of the Rh sites were empty, particularly at the beginning, where transport limitations were stronger. The most abundant surface species was CO(s).

In the literature, the compositional differences between bulk and BL often have been ascribed solely to the different transport

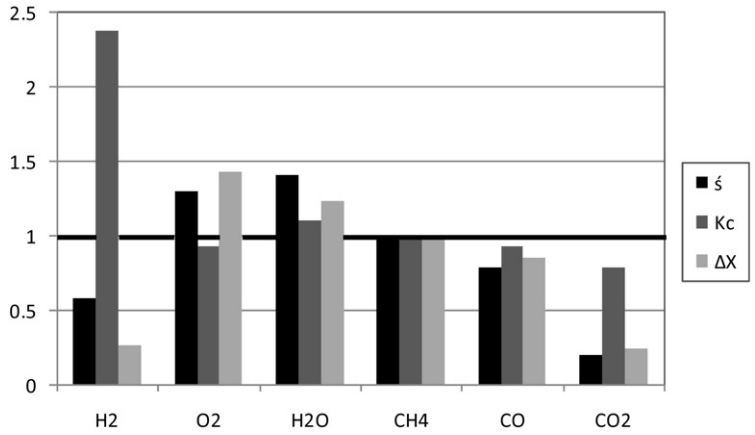

Fig. 10. Difference between bulk and superficial mole fractions (ΔX), transport coefficient (K_C) and production rate ($\dot{s}$) for each species, all scaled with respect to the values of CH_4.

coefficients of the species. But in fact, the limitations are strong for both species of low diffusivity and species with high net production rates. Indeed, transport phenomena are highly dependent on the actual rate of reaction of a species. Our findings caution against using the Chilton–Colburn analogy for reaction systems with fast heterogeneous kinetics.

Notation

bold	vectors
c_P	bulk gas specific heat, $J\,kg^{-1}\,K^{-1}$
$c_{P,S}$	solid specific heat, $J\,kg^{-1}\,K^{-1}$
D_i	species molecular diffusivity, $m^2\,s^{-1}$
d_{pore}	pore diameter, m
f	tortuosity factor
h	species enthalpy, $J\,kmol_i^{-1}$
ΔH_r^0	enthalpy of reaction, $J\,kmol^{-1}$
K	extinction coefficient, m^{-1}
K_C	mass transfer coefficient, $m\,s^{-1}$
K_T	heat transfer coefficient, $W\,m^{-2}\,K^{-1}$
L	each monolith length, m
$\dot{s}$	species production rate by surface reaction, $kmol_i\,m^{-2}\,s^{-1}$
S_V	geometric surface to void volume, $S_V = 4/d_{pore}$, m^{-1}
S'_V	geometric surface to bed volume, $S'_v = S_v \cdot \varepsilon$, m^{-1}
t	time, s
T_G	bulk gas temperature, K
T_S	solid temperature, K
v	interstitial velocity, $m\,s^{-1}$
W	molar mass, $kg_i\,kmol_i^{-1}$
X_G	bulk mole fractions, $kmol_i/kmol_{tot}$
X_{BL}	BL mole fractions, $kmol_i/kmol_{tot}$
Y_G	bulk mass fractions, kg_i/kg_{tot}
Y_{BL}	BL mass fractions, kg_i/kg_{tot}
z	axial coordinate, m

Greek letters

ε	foam porosity, V_{void}/V_{bed}
η	viscosity, $kg\,m^{-1}\,s^{-1}$
λ	bulk gas thermal conductivity, $W\,m^{-1}\,K^{-1}$
λ_S	solid thermal conductivity, $W\,m^{-1}\,K^{-1}$
ρ_G	bulk gas density, $kg\,m^{-1}$
ρ_{BL}	boundary layer gas density, $kg\,m^{-1}$
ρ_S	solid density, $kg\,m^{-1}$
σ	Stefan–Boltzmann constant, $W\,m^{-2}\,K^{-4}$

Dimensionless numbers

Nu'	$\frac{K_T}{S'_V \lambda_G}$
Pe_M	$Re \cdot Sc$
Pe_T	$Re \cdot Pr$
Pr	$\frac{\eta \cdot c_P}{\lambda}$
Re	$\frac{G}{\eta S_V}$
Re'	$\frac{G}{\eta S'_V}$
Sc	$\frac{\eta}{\rho \cdot D}$
Sh'	$\frac{K_C}{S'_V D}$

References

[1] C. Appel, J. Mantzaras, R. Schaeren, R. Bombach, A. Inauen, N. Tylli, M. Wolf, T. Griffin, D. Winkler, R. Carroni, Proc. Combust. Inst. 30 (2005) 2509.
[2] M. Bizzi, L. Basini, G. Saracco, V. Specchia, Chem. Eng. J. 90 (2002) 97.
[3] M. Bizzi, L. Basini, G. Saracco, V. Specchia, Ind. Eng. Chem. Res. 42 (2003) 62.
[4] M. Bizzi, G. Saracco, R. Schwiedernoch, O. Deutschmann, AIChE J. 50 (2004) 1289.
[5] P. Canu, S. Vecchi, AIChE J. 48 (2002) 2921.
[6] D. Dalle Nogare, PhD thesis, Department of Principles and Practice, University of Padova, 2008.
[7] N.J. Degenstein, PhD thesis, Department of Chemical Engineering and Materials Science, University of Minnesota, 2007.
[8] O. Deutschmann, L.D. Schmidt, AIChE J. 44 (1998) 2465.
[9] S. Eriksson, M. Wolf, A. Schneider, J. Mantzaras, F. Raimondi, M. Boutonnet, S. Järås, Catal. Today 117 (2006) 447.
[10] J.G. Fourie, J.P. Du Plessis, AIChE J. 50 (2004) 547.
[11] L. Giani, G. Groppi, E. Tronconi, Ind. Eng. Chem. Res. 44 (2005) 4993.
[12] L. Giani, G. Groppi, E. Tronconi, Ind. Eng. Chem. Res. 44 (2005) 9078.
[13] D.G. Goodwin, in: M.A. Maury, F. Teyssandier (Eds.), Proceedings of CVD XVI and EuroCVD Fourteen, Electrochemical Society, 2003, p. 155.
[14] C.T. Goralski Jr., R.P. O'Connor, L.D. Schmidt, Chem. Eng. Sci. 55 (2000) 1357.
[15] GRI-Mech 3.0, http://www.me.berkeley.edu/gri-mech.
[16] F.P. Incropera, D.P. DeWitt, Fundamentals of Heat and Mass Transfer, fifth ed., Wiley, New York, 1996.
[17] D.A. Hickman, L.D. Schmidt, AIChE J. 39 (1993) 1164.
[18] R. Horn, N.J. Degenstein, K.A. Williams, L.D. Schmidt, Catal. Lett. 110 (2006) 169.
[19] R. Horn, K.A. Williams, N.J. Degenstein, L.D. Schmidt, J. Catal. 242 (2006) 92.
[20] R. Horn, K.A. Williams, N.J. Degenstein, L.D. Schmidt, Chem. Eng. Sci. 62 (2007) 1298.
[21] R. Horn, K.A. Williams, N.J. Degenstein, A. Bitsch-Larsen, D. Dalle Nogare, S.A. Tupy, L.D. Schmidt, J. Catal. 249 (2007) 380.
[22] S.T. Kolaczkowski, Catal. Today 47 (1999) 209.
[23] D. Kunii, K. Suzuki, Chem. Eng. Sci. 10 (1967) 845.
[24] O. Levenspiel, Chemical Reaction Engineering, third ed., John Wiley and Sons, New York, 1999.
[25] M. Maestri, A. Beretta, G. Groppi, E. Tronconi, P. Forzatti, Int. J. Heat Mass Transfer 105 (2005) 709.
[26] Matlab, MathWorks.

[27] P.A. Nelson, T.R. Galloway, Chem. Eng. Sci. 30 (1975) 1.
[28] L.D. Pfefferle, Catal. Today 26 (1995) 255.
[29] R. Schwiedernoch, S. Tischer, C. Correa, O. Deutschmann, Chem. Eng. Sci. 58 (2003) 633.
[30] N.V. Vernikovskaya, L.N. Bobrova, L.G. Pinaeva, V.A. Sadykov, I.A. Zolotarskii, V.A. Sobyanin, I. Buyakou, V. Kalinin, S. Zhdanok, Chem. Eng. J. 134 (2007) 180.
[31] G. Veser, J. Fraunhammer, Chem. Eng. Sci. 55 (2000) 2271.